ELSEVIER

Contents lists available at ScienceDirect

Clinical Biomechanics

journal homepage: www.elsevier.com/locate/clinbiomech





Shear stress metrics associated with pro-atherogenic high-risk anatomical features in a carotid artery bifurcation model

Nora C. Zalud^a, Kartik V. Bulusu^a, Michael W. Plesniak^{a,b,*}

- ^a Department of Mechanical and Aerospace Engineering, The George Washington University, 800 22nd Street NW, Science & Engineering Hall, Suite 3000, Washington, DC 20052. United States
- b Department of Biomedical Engineering, The George Washington University, 800 22nd Street NW, Science & Engineering Hall, Suite 5000, Washington, DC 20052,

ARTICLE INFO

Keywords: Carotid artery bifurcation Computational fluid dynamics Time-averaged-wall-shear-stress Pre-disposed high-risk geometry

ABSTRACT

Background: Diseases associated with atherosclerotic plaques in the carotid artery are a major cause of deaths in the United States. Blood-flow-induced shear-stresses are known to trigger plaque formation. Prior literature suggests that the internal carotid artery sinus is prone to atherosclerosis, but there is limited understanding of why only certain patients are predisposed towards plaque formation.

Methods: We computationally investigate the effect of vessel geometry on wall-shear-stress distribution by comparing flowfields and wall-shear-stress-metrics between a low-risk and a novel predisposed high-risk carotid artery bifurcation anatomy. Both models were developed based on clinical risk estimations and patient-averaged anatomical features. The high-risk geometry has a larger internal carotid artery branching angle and a lower internal-to-carotid-artery-diameter-ratio. A patient-averaged physiological carotid artery inflow waveform is used.

Findings: The high-risk geometry experiences stronger flow separation in the sinus. Furthermore, it experiences a more equal flow split at the bifurcation, thereby reducing internal carotid artery flowrate and increasing atherosclerosis-prone low-velocity areas. Lowest time-averaged-wall-shear-stresses are present at the sinus outer wall, where plaques are often found, for both geometries. The high-risk geometry has significantly high, unfavorable oscillatory-shear-index values not found in the low-risk geometry. High oscillatory-shear-index areas are located at the vessels outside walls distal to the bifurcation and on the sinus wall.

Interpretation: These results highlight the effectiveness of oscillatory-shear-index, to augment classical time-averaged-wall-shear-stress, in evaluating pro-atherogenic geometry features. Furthermore, the flow split at the bifurcation is a promising clinical indicator for atherosclerosis risk as it can be directly accessed using clinical imaging, whereas shear-stress-metrics cannot.

1. Introduction

Cardiovascular diseases such as strokes and heart attacks are responsible for about 50% of deaths in the United States (Chandran et al., 2006). Over 15 million people suffer from a stroke every year. Carotid artery disease is estimated to cause up to 30% of strokes, affecting more than 500,000 people in the United States annually (Advanced Vascular Surgery, 2022; Mayfield Brain and Spine, 2022). This disease often involves the formation of atherosclerotic plaques which can, through growth and/or rupture, block blood supply to the downstream vasculature. Atherosclerosis primarily affects large- and

medium-sized blood vessels with complex geometries, such as bifurcations (Chiu et al., 1998; Dai et al., 2004; Fung, 2013) and is manifested by the local deposit of cholesterol and lipids on the arterial wall.

Wall-shear-stresses (WSS) act on the innermost layer in the vessel lumen, the endothelium flow (Hann et al., 2022). Endothelial cells are continuously exposed to WSS due to blood. Atherosclerosis is caused by the long-term exposure of endothelial cells to pathological blood flow via mechanotransduction, wherein mechanical forces are sensed and transmitted by the endothelial cells, resulting in a biomolecular response (French, 1992; Tada and Tarbell, 2005). Pathological cell response resulting in atherosclerosis occurs due to alterations in magnitude, and

E-mail address: plesniak@gwu.edu (M.W. Plesniak).

0268-0033/© 2023 Elsevier Ltd. All rights reserved.

^{*} Corresponding author at: The George Washington University, 800 22nd Street NW, Science & Engineering Hall, Suite 3000, Washington, DC 20052, United States.

temporal variation of WSS. In the affected regions disturbed flow is present, the time-averaged-WSS (TAWSS) is lower than normal (Himburg et al., 2004a, 2004b; Zalud et al., 2022) and spatial WSS-gradients are large (Barber et al., 1998; Conway et al., 2009; Ravensbergen et al., 1998; Rouleau et al., 2010). The endothelium experiences a complex multi-directionality of the WSS. Thus, the recent introduction of additional WSS-based quantities, such as relative residence time (Himburg et al., 2004a, 2004b), (Peiffer et al., 2013b) and WSS-topological-skeleton (Arzani and Shadden, 2018; Mazzi et al., 2020), allows a more thorough atherosclerosis-risk-assessment (Peiffer et al., 2013a; Wang et al., 2013). This study focuses on TAWSS and OSI due to their broad applicability across disciplines.

The carotid artery bifurcation (CAB) is located in the neck. It originates from the common carotid artery (CCA) and divides into the internal carotid artery (ICA) and external carotid artery (ECA). The branching causes the axial flow to follow a curved path, leading to the formation of secondary flows and flow separation, causing low-WSS at the outer walls. The ICA sinus distal to the branching point is prone to plaque formation.

In literature reporting state-of-the-art CFD-simulations, simplified and patient-specific geometries of CAB are common. The use of patientaveraged geometries allows conclusions to be drawn regarding general flow phenomena (Ku et al., 1985). Steady flow simulations are found extensively in literature (Bharadvaj et al., 1982; Gijsen et al., 1999; Nagargoje and Gupta, 2020). Physiological-pulsatile inflow waveforms are commonly used, often in combination with patient-specific geometries (Stroud et al., 2002). Most studies use either "healthy" geometries (Zhou et al., 2020) or "diseased" stenosed geometries (Bouteloup et al., 2020). The "diseased" geometries incorporate a local narrowing in the vessel diameters (due to plaque build-up). Non-diseased geometries are typically modeled on patient-averages without emphasis on patientcohort predisposition towards plaque formation. We are unaware of any published investigations of flow fields and WSS distributions in different non-diseased, non-stenosed geometries that are statistically expected to show plaque accumulation in the future. We hypothesize that CAB in patients prone to atherosclerosis formation experience different flowfields and WSS distributions than present in vessels of healthy patients.

Nguyen et al. (2008) correlated an increased atherosclerosis-risk with asymmetric bifurcation angles. Previous studies on carotid artery-related flows point to the observation of flow separation regions in the ICA sinus (Augst et al., 2007; Gijsen et al., 1999; Kumar et al., 2020; Li et al., 2019; Lopes et al., 2019; Morbiducci et al., 2011; Perktold et al., 1991). Bifurcation angle has a strong influence on the flowfield, with larger bifurcation angles resulting in larger regions of nonaxial WSS at the outer walls (Ku et al., 1985). Due to its direct connection to mechanotransduction, WSS and TAWSS are the most investigated. In addition, oscillatory-shear-index (OSI) can be correlated to atherosclerosis-risk (He and Ku, 1996; Himburg et al., 2004a).

As patient-averaged flow studies typically do not emphasize the atherosclerosis-risk of the patient-cohort, this study seeks to elucidate the flowfields and shear-stress distributions in a non-stenosed, statistically pro-atherogenic vessel model. Thus, the novelty of this study is the design of a patient-averaged CAB geometry combining all main geometrical risk factors clinically known to be present in a patient cohort at high atherosclerosis formation risk. By using patient-averaged geometries we are able to gain fundamental knowledge of the flow effects in a 'typical' high-risk patient cohort. Further, the combination of all 'typical' geometrical risk factors into one model allows the investigation of their combined effect on pro-atherogenic shear-stress-metrics.

In order to fill this knowledge gap, we have analyzed and compared flow and WSS between a statistically low-risk and a high-risk (non-stenotic, pro-atherogenic) geometry. It can be hypothesized that specific geometrical features have significant effects on the hemodynamics and thus on pro-atherogenic shear-stress-metrics. A three-dimensional CFD-simulation with a Newtonian fluid approximation and an unsteady

physiological inflow waveform was performed. This study will correlate a high-risk geometry to differences in flowfields, TAWSS and OSI.

2. Methods

2.1. Carotid artery bifurcation geometry

It is estimated that only 2-8% of the population is affected by a carotid stenosis over 50% severity (Park et al., 2012). Thus, the average person will not form atherosclerosis resulting in increased stroke risk. The high-risk population can be identified by distinct geometrical vessel features, among others. The main anatomical geometric risk-factors clinically identified were (i) an increased bifurcation angle, specifically an increased ICA angle, and (ii) a reduced ICA/CCA diameter ratio (Phan et al., 2012; Spanos et al., 2017; Thomas et al., 2005). To investigate the role of geometry in the onset of atherosclerosis, two threedimensional CAB geometries are designed, a 'low-risk' and a 'highrisk' geometry. The 'low-risk' geometry is representative of a statistically healthy patient with less predisposition towards carotid artery atherosclerosis. The 'high-risk' CAB geometry is associated with an increased clinically relevant risk for carotid artery atherosclerosis. The term 'high-risk' in the following will refer to a CAB geometry characterized by having the aforementioned geometrical risk factors that are clinically known to increase a patient's risk for atherosclerosis formation.

2.1.1. Low-risk geometry

The 'low-risk' geometry is based on physiological averages of healthy volunteers (Goubergrits et al., 2022; Marshall et al., 2004; Tada and Tarbell, 2005). The bifurcation angle is symmetric 60°, the inlet CCA diameter is 6.5 mm, the ICA sinus is included (Fig. 1a). The CCA to ICA diameter is reduced continually, leading to continuous tapering of the CCA towards the bifurcation; the CCA length is 19.5 mm. Exit lengths were added at the ends of the ICA and ECA to prevent non-physical reverse flow at the exits and improve convergence according to Cox (2018).

2.1.2. Pre-disposed high-risk geometry

The 'high-risk' geometry is based on physiological patient averages with increased pre-disposed geometrical risk for carotid atherosclerosis. The model is designed based on the low-risk geometry, where CCA and ECA dimensions were kept unchanged, but the two main geometrical risk factors clinically known to be associated with high atherosclerosis risk were changed based on clinical data. First, the ICA bifurcation angle was increased to 45° (Phan et al., 2012), resulting in an asymmetric bifurcation angle. Second, the ICA/CCA diameter ratio was reduced to 0.5 in comparison to the 'low-risk model' by reducing the ICA diameter. (Spanos et al., 2017) (Fig. 1b) (Table 1). The design of this novel predisposed high-risk geometry, based on the healthy CAB and incorporating the main clinical geometrical risk factors, allows a unique study of those clinically typically combined risk factors influence on the flow fields.

2.2. Computational fluid dynamics (CFD)

Three-dimensional flow and wall-shear-stress (WSS) analysis is done using CFD. ANSYS® FLUENT Academic Research Mechanical Release 2021-R1 was used to solve the Navier-Stokes-equations employing a finite-volume method using a pressure-based solver under pulsatile laminar-flow conditions. ANSYS® meshing and ANSYS® FLUENT were used to discretize the domain and post result processing, respectively.

2.2.1. Spatial and time discretization

The domain was discretized using tetrahedral meshing in the core region and boundary layer meshing close to the vessel wall with total 2,080,502 mesh-elements in the domain. High accuracy of the spatial

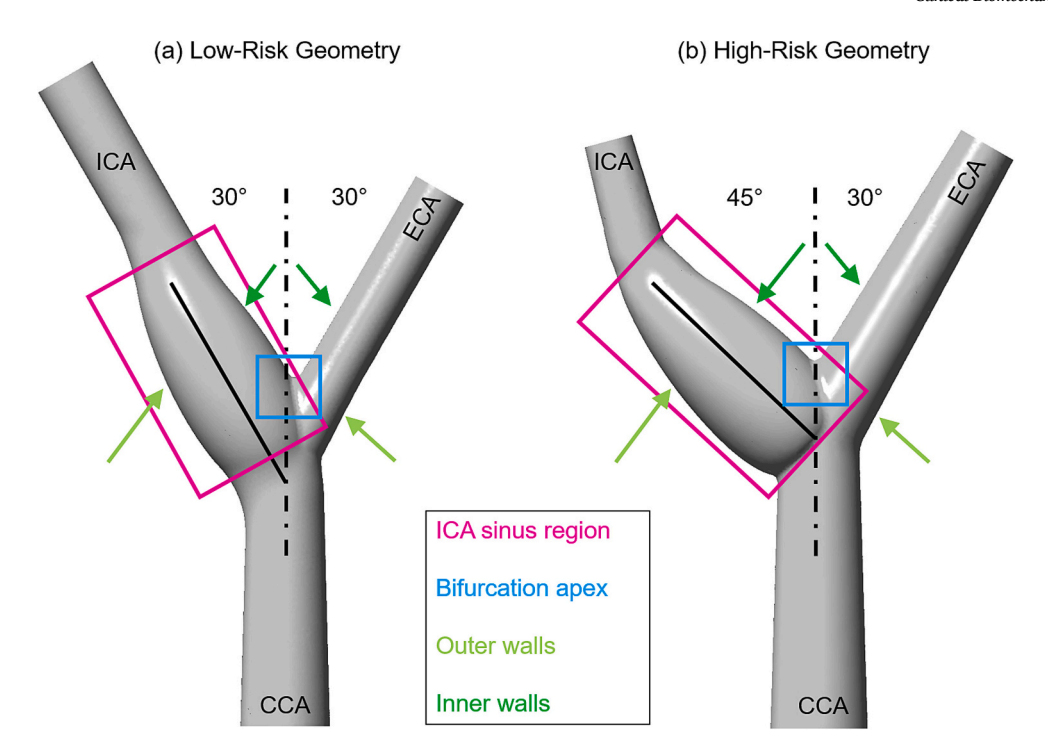


Fig. 1. Model geometries without and with geometric risk factors. (a) Low-risk geometry with symmetric 30° branching angle. (b) High-risk geometry with asymmetric branching angle, increased 45° ICA angle and a 0.5 ICA/CCA diameter ratio that is lower than for the low-risk model.

Table 1Main anatomical geometric risk factor comparison between low-risk and high-risk geometry models.

	Low-risk geometry	High-risk geometry
Branching angle total	60°	75°
Branching angle ICA	30°	45°
ICA/CCA diameter ratio	0.7	0.5

discretization is guaranteed by performing a mesh independence study and observing local velocity (Fig. 2a) and WSS dependence on the number of mesh elements. The accuracy of the core mesh was validated using bulk flow properties like mass flow and velocity, whereas the accuracy of the boundary layer mesh was investigated using wall bounded properties. In a first step, a coarse core mesh was set and kept constant while boundary layer properties, especially the layer thickness and number of mesh layers were varied until grid independence was

attained. In a second step, the validated boundary layer mesh was kept constant, while the core mesh was refined to achieve independence of bulk flow properties on the volume mesh. This two-step approach allowed the independence of bulk flow properties as well as wall metrics by keeping computational cost low. The simulations are run for several cycles of the physiological flowrate waveform until a cycle-to-cycle repeatability of flow conditions is achieved. Data are analyzed during the third physiological cycle in this study. Accuracy of temporal discretization was achieved by choosing a fixed time step of 0.0000625 s that ensured the maximum Courant-Friedrichs-Lewy (CFL) number remains smaller than 1.

2.2.2. Boundary conditions

The CCA provides the velocity inlet condition, mass outflow is based on physiological averages, and no-slip boundary conditions are applied at the rigid walls. Inflow rates reach a peak Reynolds-number (Re) of 1530, while the mean Re is 385, where Re is defined as flow velocity

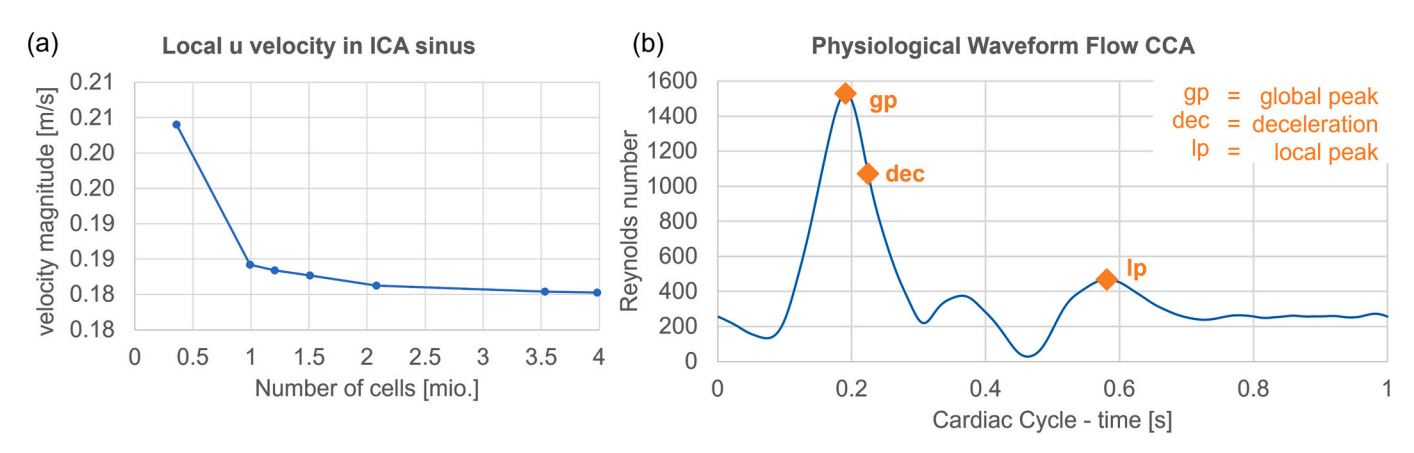


Fig. 2. Meshing and physiological inflow waveform. (a) Mesh independence study showing achievement of sufficient accuracy while reducing boundary layer and core mesh cells. (b) Physiological inflow waveform at the CCA used as velocity inflow boundary condition. Representing one cardiac cycle with period of 1 s. Highlighted with orange diamonds are characteristic moments during the cardiac cycle.

multiplied by CCA diameter and divided by the kinematic viscosity. The flow is Re-matched to physiological blood-flow by using a kinematic viscosity of 6.95 • 10^{-7} m^2/sec , allowing improved comparability with cell studies investigating mechanotransduction. Furthermore, a Newtonian fluid assumption is used because carotid artery flow experiences only minor non-Newtonian effects (Boyd and Buick, 2007). The physiological-pulsatile waveform used at the velocity inlet represents a patient-average and is based on Holdsworth (1999); the digitized waveform function developed in our lab is used (Bulusu and Plesniak, 2013; Glenn et al., 2012; Najjari and Plesniak, 2016; Peterson and Plesniak, 2008). The waveform period (T) is a physiological 1 s, corresponding to 60 bpm (Fig. 2b). A spatially uniform inflow profile is applied at the velocity inlet where the inflow magnitude is described by the time-dependent physiological inflow waveform, for both geometries. Analysis focuses on diastolic flow phenomena characteristic-instances-of-time ranging from peak flowrate acceleration to diastolic flowrate peak (Bulusu and Plesniak, 2018; Cox et al., 2019). The mass outflow at ICA and ECA is controlled through a resistive outflow boundary condition, that is chosen due to its numerical robustness and nearly identical behavior as classical three-element Windkessel models (Capuano et al., 2019). The resistive outlet conditions follow $\Delta p = R \bullet Q$, where Δp is the pressure drop in Pascals, R is the vascular resistance in $[Pa \bullet s/m^3]$ and Q is the volume flowrate in m^3/s . The outlet pressure drops are time dependent due to their dependence on the volume flow rate, given by the inflow waveform described above and their respective resistances. This method allows control of the flow split between the two branches to match clinical data. Resistances for ICA and ECA were iteratively changed until ICA volume outflow matched patient-averaged data (Ford et al., 2005), while ECA outflow was set to be CCA inflow minus ICA outflow. The vascular resistances for the ICA and ECA are $R_{ICA} = 1.5 \bullet 10^6 \, Pa \bullet s \bullet m^{-3}$ and $R_{ECA} = 11 \bullet 10^6 \, Pa$ • $s \cdot m^{-3}$, respectively, for the low-risk as well as high-risk geometry.

2.2.3. TAWSS and OSI

Shear-stress drives the mechanotransduction process and thus WSS-metrics provide an indicator of cell response. To capture the stresses on vascular cells over the entire cardiac cycle TAWSS is calculated according to Eq. (1a) & (1b), where T is the period of one cardiac cycle with a duration of one second, the limits of integration, \mathbf{t}_2 to \mathbf{t}_1 indicate the third cardiac cycle, i.e. $\mathbf{t}_1=2$ s and $\mathbf{t}_2=3$ s, $|\overrightarrow{\tau_w}|$ the absolute local WSS, D_{CCA} the CCA diameter, μ the dynamic viscosity and $u_{CCA, mean}$ the averaged mean inflow velocity.

$$TAWSS = \frac{1}{T} \bullet \int_{t_1}^{t_2} |\overline{\tau_w}| dt$$
 (1a)

$$TAWSS_{norm} = \frac{1}{T} \bullet \int_{t_{i}}^{t_{2}} |\overrightarrow{\tau_{w}^{*}}| dt, \text{ where } |\overrightarrow{\tau_{w}^{*}}| = |\overrightarrow{\tau_{w}}| \bullet \frac{D_{CCA}}{\mu \bullet u_{CCA,mean}}$$
(1b)

Another commonly used metric to describe shear-stresses correlated to mechanotransduction is the oscillatory-shear-index (OSI) (eq. 2) (He and Ku, 1996), where OSI ranges from zero to 0.5.

$$OSI = 0.5 \bullet \left(1 - \frac{\left| \overrightarrow{\tau}_{mean} \right|}{TAWSS} \right); where \overrightarrow{\tau}_{mean} = \frac{1}{T} \bullet \int_{t_1}^{t_2} \overrightarrow{\tau}_w dt$$
 (2)

3. Results

The results show flowfields and WSS in the low- and high-risk

geometry, focusing on two main areas (Fig. 1), the sinus and the bifurcation apex, and three characteristic instances in the pulsatile cycle (Fig. 2b). Streamwise velocity showcases important flow features, such as separation regions and vortices. Instantaneous WSS plots highlight stresses acting on the endothelium. This is followed by the analysis of TAWSS and OSI for both geometries. Data-instances in the cardiac cycle are indicated in the insets by the orange diamond on the blue pulsatile waveform.

3.1. Streamwise velocity

Fig. 3 shows the velocity magnitude and vectors plotted on the vessel's radial center plane. Fig. 3(i) shows the flowfield for the inflowrate peak at t/T = 2.19, and Fig. 3(ii) represents the inflow deceleration at t/T = 2.27. The low- and high-risk geometries are shown in subfigures (a) and (b), respectively.

For the low-risk geometry at the flowrate peak (t/T=2.19) small separation zones with low velocity along the sinus inner and outer walls are present (Fig. 3(i)a). The high-risk geometry exhibits a similar flow pattern, but contains a significantly larger, low-velocity separation zone at the sinus outer wall. The high-risk geometry additionally, shows a low-velocity vortex core in the sinus. It is located adjacent to the low-velocity core of the flow separation, closer to the vessel's axial center axis (Fig. 3(i)b).

During the inflow deceleration phase (t/T = 2.27) a high-velocity jet forms towards the bifurcation apex for both geometries (Fig. 3(ii)). Left and right of this jet, a counter-rotating vortex pair (indicated by the dark arrows in Figs. 3(ii)a&b) is observed in the ICA and ECA. For the low-risk geometry very little flow exits the ECA, most streams through the ICA (Fig. 3(ii)a). A vortex in the sinus counteracts the separation zone's lowvelocity field and increases the velocity throughout most of the sinus. This vortex streams in a direction opposite to the axial flow on the ICA outer sinus wall side and leaves only a small low-velocity separation zone at the upstream end of the sinus' outer wall. For the high-risk geometry, the jet splits more equally between ECA and ICA, resulting in less flow through the ICA (Fig. 3(ii)b). The counter-rotating vortex pair occupies larger areas in the sinus. It also increases the velocity at the outer wall, but a larger low-velocity area remains in the sinus as the vortex center is closer to the inner sinus wall compared to the low-risk geometry. There are lower retrograde flow velocity magnitudes present close to the sinus's outer wall for the high-risk geometry compared to the low-risk geometry.

3.2. Instantaneous WSS

At the inflow peak flowrate (t/T = 2.19) a band shaped high-WSS region (indicated by arrows) with WSS vectors opposite to the axial flow is observed for both geometries (Fig. 4(i)). It is positioned at the most upstream portion of the sinus. Just downstream, a low-WSS region is present, which has an approximately 40% larger area for the high-risk geometry.

In the inflow deceleration phase (t/T = 2.27), the high-WSS region expands further towards the CCA at the side walls of the sinus. The existence of a vortex and its influence on the WSS can be seen for both geometries, as the WSS vectors follow a circular path at the sinus side walls (Fig. 4(ii)a&b, arrow). Fig. 4(iii) shows that the high-WSS region is positioned where the presence of a vortex can be discerned from the curved three-dimensional streamlines. For the high-risk geometry, a low-WSS band forms at the inner sinus wall spreading between the two vortex areas (Fig. 4(ii)b). Furthermore, at the outer sinus wall, right at the branching point, the high-risk geometry contains a large, low-WSS

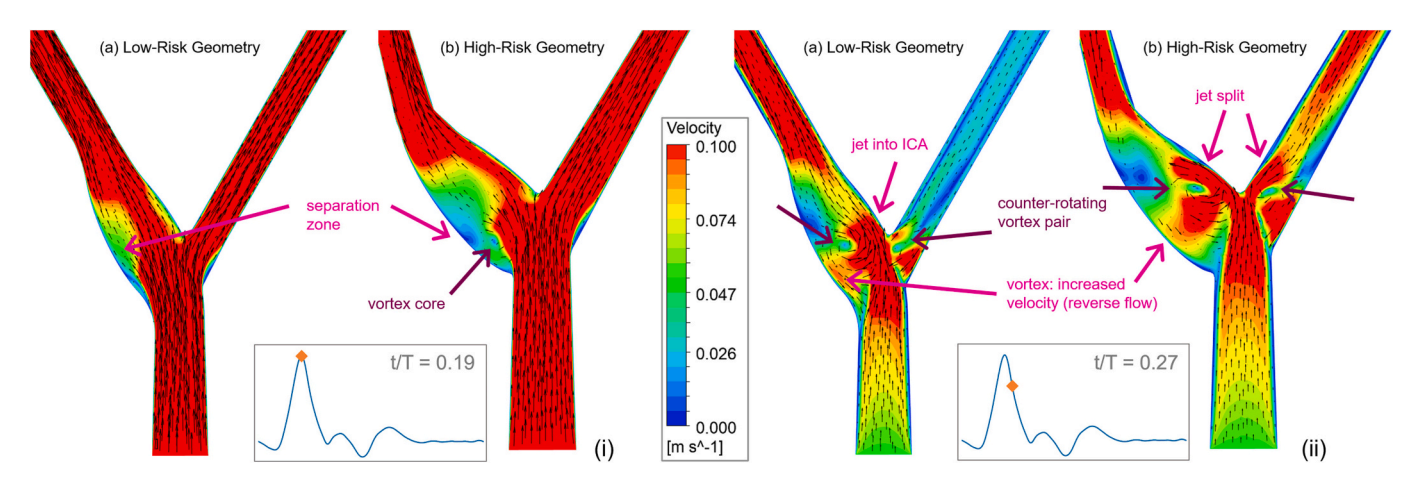


Fig. 3. Flowfield comparison in peak and decelerating inflow between low- and high-risk geometry. Figure shows the velocity magnitude (color bar) in the vessel's axial center plane and black velocity vectors for (a) the low-risk geometry and (b) high-risk geometry. (i) Moment during the third cycle at t/T = 2.19, when inflow velocity waveform is at its maximum (as indicated by the orange diamond on the blue waveform curve). Low velocity flow-separation zone is found in the ICA sinus for both geometries, being much larger for the high-risk geometry. (ii) Moment during the third cycle at t/T = 2.27, when inflow velocity waveform in its deceleration phase (as indicated by the orange diamond on the blue waveform curve). A high velocity jet forms towards the bifurcation apex, splitting more equally between ICA and ECA in case of the high-risk geometry. A counter-rotating vortex pair forms next to the jet. It increases the velocity close to the sinus outer wall and is much stronger for the low-risk geometry then for the high-risk geometry. (For interpretation of the references to color in this figure legend, the reader is referred to the web version of this article.)

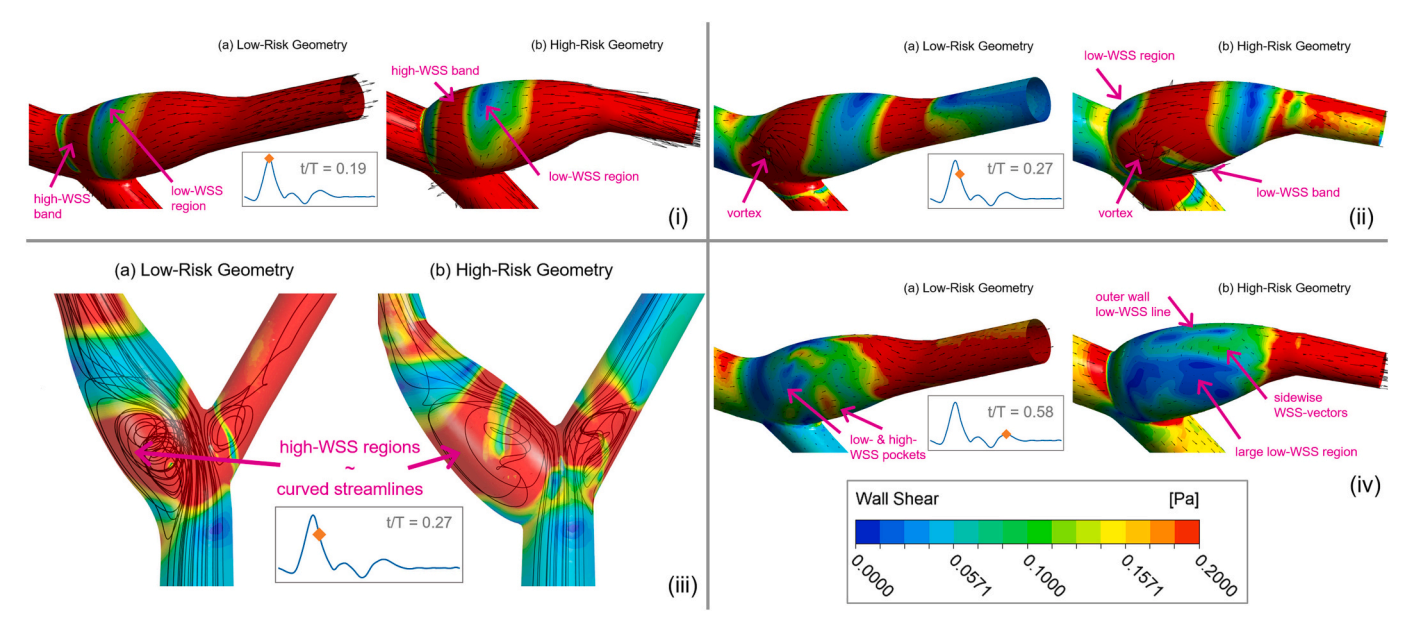


Fig. 4. Instantaneous wall shear stress distribution during physiological cycle as comparison between low- and high-risk geometry. WSS magnitude (color bar, shown bottom right in iv for all) – solid color for (i), (ii) and (iv), partly transparent for (iii) - and black velocity vectors (for i, ii, iv) and three-dimensional streamlines (for iii) for (a) the low-risk geometry, and (b) high-risk geometry respectively. Instantaneous moments given as "time value" as well as indicated by the orange diamond on the blue waveform curve. (i) Moment during the third cycle at t/T = 2.19, when inflow velocity waveform is at its maximum. High WSS band forms on ICA outer sinus wall pointing in opposite direction to the main flow for both geometries. The high-risk geometry experiences a larger low WSS area at the sinus outer wall. (ii) Moment during the third cycle at t/T = 2.27, when inflow velocity waveform is in its deceleration phase. WSS vectors pointing in a circular pattern, caused by a vortex can be seen at sinus side walls for both geometries. The high-risk geometry experiences a larger high-WSS region on the sinus wall with a low-WSS band at the sinus inner wall. Furthermore, it experiences lower WSS at the sinus outer wall directly downstream of the branching point. (iii) Moment during the third cycle at t/T = 2.27, when inflow velocity waveform is in its deceleration phase. The high-wSS band is positioned where a vortex signature is discernable from the curved, three-dimensional streamlines. (iv) Moment during the third cycle at t/T = 2.58, when inflow velocity waveform is at its local maximum during diastolic phase. Low-risk geometry shows several high- and low- WSS pockets on the sinus surface. For the high-risk geometry a significantly larger area is occupied with low WSS at the sinus side walls. WSS vectors are pointing from the 'outer wall low WSS line' towards the low-WSS pockets at the ICA sinus side walls. (For interpretation of the references to color in this figure legend, the reader is referred

region that is not present in the low-risk geometry (Fig. 4(ii)a).

Towards the end of the inflow cycle (t/T=2.58) there are several small high- and low-WSS pockets present for the low-risk geometry distributed over the sinus wall (Fig. 4(iv)a). WSS vectors on the sinus wall are aligned with the axial flow direction. In contrast, in the high-

risk geometry's sinus, there are no high-WSS pockets present and a significantly larger area is occupied with low-WSS at the sinus side walls. WSS vectors point sidewise, from the 'outer wall low-WSS line' towards the low-WSS pockets (Fig. 4(iv)b) rather than in the axial flow direction.

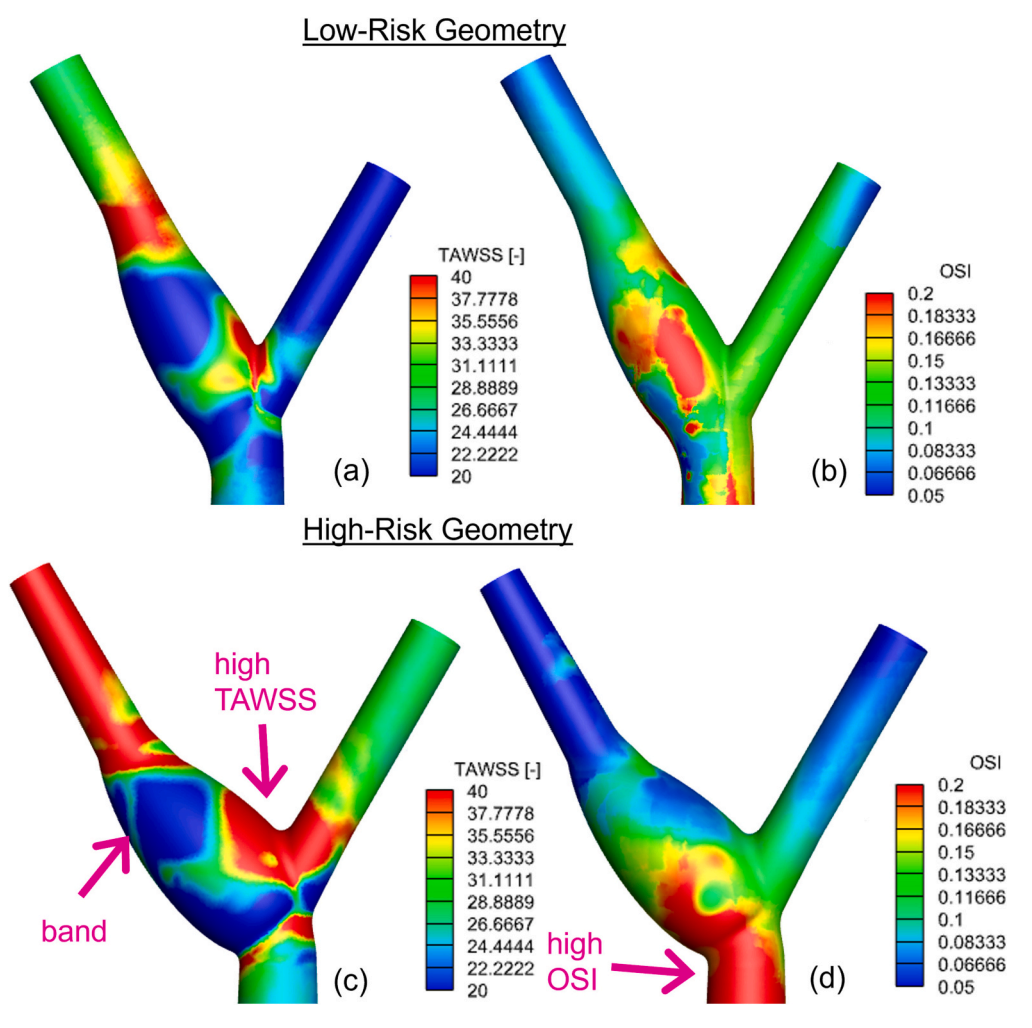


Fig. 5. TAWSS and OSI for the low-risk and high-risk geometry on the top (a&b) and bottom (c&d) row, respectively. Dimensionless TAWSS (a&c) and OSI (b&d) are shown in the left and right column, respectively. TAWSS is low in the sinus for both geometries. TAWSS is higher at the bifurcation apex or the high-risk geometry and low sinus TAWSS interrupted by a high WSS band. OSI is low for the low-risk geometry in the CCA close to the bifurcation and at the sinus's outer wall and significantly higher in the highrisk geometry specifically at the ICA sinus's outer wall close to the bifurcation point.

3.3. TAWSS and OSI

Fig. 5 shows TAWSS and OSI for the low-risk and high-risk geometry on the top and bottom row, respectively. Dimensionless TAWSS and OSI are shown in the left and right columns, respectively.

TAWSS exhibits similar patterns for both geometries. Its dimensionless magnitude is 23–33 [–] (Fig. 5a&c) through the CCA and ECA, and higher in the ICA downstream of the sinus, as well as at the bifurcation apex (Fig. 5a&c, red). The high TAWSS in the ICA downstream of the sinus is expected due to a significant bulk velocity increase arising from the reduced vessel diameter (and flow area) distal to the sinus. TAWSS is lowest at the bifurcation point at ICA and ECA outer walls, and at the sinus wall (Fig. 5a&c, dark blue). In the low-risk geometry a low-TAWSS band can be observed in the downstream half of the sinus. For the high-risk geometry this low-TAWSS band is interrupted by a thin high-TAWSS band (Fig. 5c). Furthermore, a much larger, high-TAWSS region is observed around the bifurcation apex.

The low-risk geometry experiences a generally low OSI, where lowest OSI regions occur around the sinus (Fig. 5b). The high-risk geometry experiences much higher OSI in the CCA, ICA and ECA (Fig. 5d). The increased OSI in the CCA for the high-risk geometry is attributable to the tapering of the CCA, the increased flow resistance from the bifurcation, and characteristics of the physiological pulsatile inflow waveform. In the inflow deceleration phase, development of Womersley-type velocity profile is observed, which contains reversed flow in the boundary layer (opposite to the primary bulk flow direction), resulting in increased OSI. At a major region of interest, the sinus' outer wall, OSI is up to 200% higher for the high-risk geometry, compared to

the low-risk case. High-OSI regions are denser around the bifurcation and OSI gradually diminishes in downstream direction of the ICA and ECA. The vessel outer walls experience larger areas of high-OSI than the vessel inner walls. Generally, higher OSI occurs at the vessel outer walls, where the TAWSS is low.

4. Discussion

We will compare and discuss streamwise flow structures, instantaneous WSS, TAWSS and OSI distributions for the low- and high-risk geometries.

4.1.1. Streamwise velocity fields

The high-risk geometry, due to its larger ICA angle and sinus volume, experiences less flow through the ICA and larger low-velocity regions in the sinus due to flow separation having greater extent compared to the low-risk case. For both geometries, the ICA vortex has a desirable effect as it increases the velocity magnitude close to the sinus outer wall even though it causes retrograde flow. For the high-risk geometry, the counter-rotating vortex pair is closer to the inner walls than for the low-risk geometry, reducing its velocity-increasing effect (via Biot-Savart induced velocity) at the ICA outer sinus wall.

A significant difference between the two geometries is the flow split of the fluid jet into ICA and ECA. Whereas almost the entire jet streams into the ICA for the low-risk geometry, leading to a high flow rate and large, high-velocity regions, the jet splits more equally between ICA and ECA for the high-risk geometry. This jet split reduced the flow rate through the ICA, resulting in larger atherosclerosis-prone low-velocity areas. The presence or absence of a flow split would be directly identifiable through flow-MRI imaging without the need for patient-specific modeling and calculation of shear stress metrics and thus providing a decision-making parameter directly assessable to clinicians. The jet development and resulting flow split is significantly different between a healthy low-risk and pre-disposed high-risk vessel geometry. This jet behavior is responsible for the subsequent effects of decreased flow rate through the ICA, resulting in larger low-velocity, low-WSS regions. These regions are associated with TAWSS and OSI linked to increased atherosclerosis risk.

4.1.2. Instantaneous WSS

Both geometries have lower WSS magnitudes in the sinus than in the CCA or the ICA downstream of the sinus. Due to the larger branching angle, the high-risk geometry experiences a larger low-WSS region. Generally, the high-risk geometry experiences lower WSS in the sinus over the highlighted instants of the cardiac cycle. Furthermore, the WSS vectors are primarily aligned with the CCA-ICA axial flow direction for the low-risk geometry. In contrast, flow in the high-risk geometry sinus is more multi-directional, with WSS vectors pointing sidewards due to vortices present in that region.

4.1.3. TAWSS and OSI

TAWSS varies significantly over the surface for both geometries. High-TAWSS regions are, as expected, present at the bifurcation apex and the ICA downstream of the sinus. The outer vessel walls at the bifurcation point and the sinus experience the lowest TAWSS's. Notably, the TAWSS distributions for the low-risk and high-risk geometries look relatively similar, even though the high-risk geometry shows a larger low-TAWSS region in the most upstream top part of the ICA sinus. This suggests that TAWSS alone is not a sufficient parameter to relate a certain geometry with predisposition for disease, in agreement with literature (Bantwal et al., 2022; Hashemi et al., 2021; Moradicheghamahi et al., 2020). There are, however, significant differences in OSI fields observed between the two geometries. The high-risk geometry has large areas of unfavorable (high) OSI that is associated with increased plaque formation risk. These high-OSI values were observed only in the high-risk geometry, concentrated around the outer bifurcation walls and the ICA outer sinus wall, whereas the low-risk geometry experiences low OSI throughout the vessel. The high-risk geometry contains high values of OSI in the downstream-most region of the CCA immediately upstream of the bifurcation, which agrees with clinical data (Steinman et al., 1997) of a patient-specific simulation of a carotid artery bifurcation with similar geometrical features, namely a high ICAasymmetric branching angle.

Drawing a clear conclusion on increased risk based on TAWSS alone was shown to be difficult because both cases contain qualitatively similar TAWSS characteristics. On the other hand, a clear distinction between the low-risk geometry having low OSI and the high-risk geometry experiencing high OSI is apparent. The significance of OSI analysis to determine atherosclerosis-risk found in this study agrees with literature (Bantwal et al., 2022; Hashemi et al., 2021; Moradicheghamahi et al., 2020). Geometrical features of the CAB clinically related to increased atherosclerosis-risk led to increased OSI. Especially the sinus is strongly affected by these geometrical changes and shows a significant increase of OSI for the high-risk geometry. The results reveal changes in critical shear-stress-metrics, especially the OSI, when the main geometrical risk factors are present. These results support the hypothesis that specific anatomical features have significant effects on hemodynamics and thus on pro-atherogenic WSS-metrics. Our study further showed that OSI could be used as indicators of a patient's atherosclerosis risk and will be a powerful metric to support clinical decision making. The observed differences in TAWSS and OSI can be

used for identification of high-risk-patients based on these shear-stressmetrics in a later clinical stage.

4.1.4. Limitations

In this study, two characteristic geometries have been investigated with respect to the influence of their geometrical differences on atherosclerosis-prone shear-stress-metrics. To reduce the complexity and variability of patient-specific geometries, patient-averaged geometries with the clinically reported salient features found in patients that developed stenoses were used. While this provided new insights into what difference in flow fields and shear-stress-metrics are expected between healthy and pre-disposed general anatomical features, further expansion of these findings using larger data sets, by conducting parametric studies on idealized geometries or investigating a wide range of patient-specific geometries, will augment the findings of this study.

5. Conclusion

Physiological-pulsatile-flow CFD-simulations were performed in two different patient-averaged carotid artery anatomical geometries - one "pre-disposed" associated with anatomical geometry with high-risk of disease development, the other from a low-risk, healthy population. The high-risk geometry shows increased areas of low-velocity flow separation zones resulting in low-WSS regions at the ICA sinus wall. The sinus, the location where atherosclerotic plaques are typically found, exhibited low-TAWSS for both geometries. The OSI distributions were significantly different between the low-risk and high-risk geometries. For the high-risk geometry, the OSI was of higher magnitude (up to 200%) especially around the central sinus region, which might be associated with pathological mechanotransduction. The anatomical high-risk factors such as asymmetric branching angle, larger ICA branching angle and a smaller ICA/CCA diameter ratio, all affect the sinus region shape. And they were found to cause an unfavorable WSS distribution in the sinus, namely low-TAWSS and higher OSI. Our results highlight the significant impact of increased ICA branching angle and reduced ICA/ CCA diameter ratio on pro-atherosclerotic shear-stress-metrics. Furthermore, this study illustrates the utility of OSI, to augment classical TAWSS, as indicator of atherosclerosis risk. A significant difference between the two geometries is the jet flow split between ICA and ECA. Whereas most flow enters the ICA for the low-risk geometry, increasing the velocities in the sinus, the high-risk geometry experiences an almost equal flow split. The classical shear-stress-metrics are useful for atherosclerosis-risk prediction using patient based CFD simulations when the carotid artery bifurcation geometry is known from medical imaging (such as CT or MRI scans). The presence or absence of a jet split at the carotid artery bifurcation, on the other hand, can be visualized through flow-MRI imaging and thus might present an auspicious addition and eventual alternative to patient-specific modeling, CFD simulation and shear-stress-metric calculation. Thus, the herein reported substantial and easily discernable difference in the ICA-ECA flow split between low- and high-risk geometries represents a promising clinical indicator for atherosclerosis risk assessment.

CRediT authorship contribution statement

Nora C. Zalud: Conceptualization, Methodology, Software, Validation, Formal analysis, Investigation, Resources, Data curation, Writing – original draft, Visualization, Project administration. Kartik V. Bulusu: Conceptualization, Methodology, Supervision, Writing – review & editing. Michael W. Plesniak: Funding acquisition, Conceptualization, Methodology, Supervision, Project administration, Resources, Writing - review & editing.

Declaration of Competing Interest

The authors declare that there is no conflict of interest.

Acknowledgement

This work was supported by the National Science Foundation (CBET-1854415). The first author was further supported by the George Washington University graduate research assistantship and the Michael K. Myers Merit Scholarship. This study was completed in part with resources provided by the High-Performance Computing Cluster at The George Washington University, Information Technology, Research Technology Services.

References

- Advanced Vascular Surgery, 2022. TCAR (Carotid Revascularization). https://www.avsurgery.com/services/tcar-carotid-revascularization/.
- Arzani, A., Shadden, S.C., 2018. Wall shear stress fixed points in cardiovascular fluid mechanics. J. Biomech. 73, 145–152. https://doi.org/10.1016/j. ibiomech.2018.03.034.
- Augst, A.D., Ariff, B., Thom, S.A.G.M., Xu, X.Y., Hughes, A.D., 2007. Analysis of complex flow and the relationship between blood pressure, wall shear stress, and intimamedia thickness in the human carotid artery. Am. J. Phys. Heart Circ. Phys. 293, 1031–1037. https://doi.org/10.1152/ajpheart.00989.2006-Background.
- Bantwal, A., Singh, A., Menon, A.R., Kumar, N., 2022. Hemodynamic study of blood flow in the carotid artery with a focus on carotid sinus using fluid-structure interaction. J. Fluids Eng. Trans. ASME 144 (2). https://doi.org/10.1115/1.4051902, 021403.1-021403.11.
- Barber, K.M., Pinero, A., Truskey, G.A., 1998. Effects of recirculating flow on U-937 cell adhesion to human umbilical vein endothelial cells. Am. J. Phys. Heart Circ. Phys. 275 (2), H591–H599.
- Bharadvaj, B.K., Mabon, R.F., Giddens, D.P., 1982. Steady flow in a model of the human carotid bifurcation. Part II—laser-Doppler anemometer measurements. J. Biomech. 15 (5), 363–378.
- Bouteloup, H., de O Marinho, J.G., Chatpun, S., Espino, D.M., 2020. Computational analysis to predict the effect of pre-bifurcation stenosis on the hemodynamics of the internal and external carotid arteries. J. Mech. Eng. Sci. 14 (3), 7029–7039. https:// doi.org/10.15282/jmes.14.3.2020.05.0550.
- Boyd, J., Buick, J.M., 2007. Comparison of Newtonian and non-Newtonian flows in a two-dimensional carotid artery model using the lattice Boltzmann method. Phys. Med. Biol. 52 (20), 6215–6228. https://doi.org/10.1088/0031-9155/52/20/009.
- Bulusu, K.V., Plesniak, M.W., 2013. Secondary flow morphologies due to model stent-induced perturbations in a 180° curved tube during systolic deceleration. Exp. Fluids 54 (3), 1–13. https://doi.org/10.1007/s00348-013-1493-7.
- Bulusu, K.V., Plesniak, M.W., 2018. Insights on arterial secondary flow structures and vortex dynamics gained using the MRV technique. Int. J. Heat Fluid Flow 73, 143–153. https://doi.org/10.1016/j.ijheatfluidflow.2018.08.002.
- Capuano, F., Loke, Y.H., Balaras, E., 2019. Blood flow dynamics at the pulmonary artery bifurcation. Fluids 4 (4), 190. https://doi.org/10.3390/fluids4040190.
- Chandran, K.B., Rittgers, S.E., Yoganathan, A.P., 2006. Biofluid Mechanics the Human Circulation (1st Edition). CRC Press.
- Chiu, J.-J., Wang, D.L., Chien, S., Skalak, R., Usami, S., 1998. Effects of disturbed flow on endothelial cells. J. Biomech. Eng. 120 (1), 2–8.
- Conway, D.E., Williams, M.R., Eskin, S.G., McIntire, L.V., 2009. Endothelial cell responses to atheroprone flow are driven by two separate flow components: low time-average shear stress and fluid flow reversal. Am. J. Phys. Heart Circ. Phys. 298 (2), H367–H374.
- Cox, C., 2018. Development of a High-Order Navier-Stokes Solver Using Flux Reconstruction to Simulate Three-Dimensional vortex Structures in a Curved Artery Model [Dissertation]. The George Washington University.
- Cox, C., Najjari, M.R., Plesniak, M.W., 2019. Three-dimensional vortical structures and wall shear stress in a curved artery model. Phys. Fluids 31 (12), 121903. https://doi. org/10.1063/1.5124876.
- Dai, G., Kaazempur-Mofrad, M.R., Natarajan, S., Zhang, Y., Vaughn, S., Blackman, B.R., Kamm, R.D., García-Cardeñ, G., Gimbrone, M.A., 2004. Distinct endothelial phenotypes evoked by arterial waveforms derived from atherosclerosis-susceptible and-resistant regions of human vasculature. Proc. Natl. Acad. Sci. 101 (41), 14871–14876. www.pnas.orgcgidoi10.1073pnas.0406073101.
- Ford, M.D., Alperin, N., Sung, H.L., Holdsworth, D.W., Steinman, D.A., 2005. Characterization of volumetric flow rate waveforms in the normal internal carotid and vertebral arteries. Physiol. Meas. 26 (4), 477–488. https://doi.org/10.1088/ 0967-3334/26/4/013.
- French, A.S., 1992. Mechanotransduction. Annual review of physiology 54 (1), 135–152. Fung, V., 2013. Biomechanics: Circulation, Second edition. Springer Science & Business
- Gijsen, F.J.H., Van De Vosse, F.N., Janssen, J.D., 1999. The influence of the non-Newtonian properties of blood on the flow in large arteries: steady flow in a carotid bifurcation model. J. Biomech. 32, 601–608.
- Glenn, A.L., Bulusu, K.V., Shu, F., Plesniak, M.W., 2012. Secondary flow structures under stent-induced perturbations for cardiovascular flow in a curved artery model. Int. J. Heat Fluid Flow 35, 76–83. https://doi.org/10.1016/j.ijheatfluidflow.2012.02.005.
- Goubergrits, L., Affeld, K., Fernandez-Britto, J., Falcon, L., 2022. Geometry of the human common carotid artery. A vessel cast study of 86 specimens. Pathol. Res. Pract. 198 (8), 543–551.

- Hann, S.Y., Cui, H., Zalud, N.C., Esworthy, T., Bulusu, K., Shen, Y.L., Plesniak, M.W., Zhang, L.G., 2022. An in vitro analysis of the effect of geometry-induced flows on endothelial cell behavior in 3D printed small-diameter blood vessels. Biomater. Adv. 137 https://doi.org/10.1016/j.bioadv.2022.212832.
- Hashemi, J., Patel, B., Chatzizisis, Y.S., Kassab, G.S., 2021. Study of coronary atherosclerosis using blood residence time enhanced reader. Front. Physiol. 12, 566–566
- He, X., Ku, D.N., 1996. Pulsatile flow in the human left coronary artery bifurcation: average conditions. J. Biomech. Eng. 118 (1), 74–82.
- Himburg, H.A., Grzybowski, D.M., Hazel, A.L., LaMack, J.A., Li, X.-M., Friedman, M.H., 2004a. Spatial comparison between wall shear stress measures and procine arterial endothelial permeability. Am. J. Physiol. Heart Circ. Physiol. 286 (5), H1916–H1922.
- Himburg, H.A., Grzybowski, D.M., Hazel, A.L., Lamack, J.A., Li, X.-M., Friedman, M.H., Friedman, M.H., 2004b. Spatial comparison between wall shear stress measures and porcine arterial endothelial permeability. Am. J. Physiol. Heart Circ. Physiol. 286, 1916–1922. https://doi.org/10.1152/ajpheart.00897.2003.-A.
- Holdsworth, D.W., et al., 1999. Characterization of common carotid artery blood-flow waveforms in normal human subjects. Physiological measurement 20 (3), 219
- Ku, D.N., Giddens, D.P., Zarins, C.K., Glagov, S., 1985. Pulsatile flow and atherosclerosis in the human carotid bifurcation positive correlation between plaque location and low and oscillating shear stress. Arterioscler.: Off. J Am. Heart Assoc. Inc. 5 (3), 293–302. http://abajournals.org.
- Kumar, N., Khader, S.M.A., Pai, R., Khan, S.H., Kyriacou, P.A., 2020. Fluid structure interaction study of stenosed carotid artery considering the effects of blood pressure. Int. J. Eng. Sci. 154, 103341 https://doi.org/10.1016/j.ijengsci.2020.103341.
- Li, C.H., Gao, B.L., Wang, J.W., Liu, J.F., Li, H., Yang, S.T., 2019. Hemodynamic factors affecting carotid sinus atherosclerotic stenosis. World Neurosurg. 121, e262–e276. https://doi.org/10.1016/j.wneu.2018.09.091.
- Lopes, D., Puga, H., Teixeira, J.C., Teixeira, S.F., 2019. Influence of arterial mechanical properties on carotid blood flow: comparison of CFD and FSI studies. Int. J. Mech. Sci. 160, 209–218. https://doi.org/10.1016/j.ijmecsci.2019.06.029.
- Marshall, I., Papathanasopoulou, P., Wartolowska, K., 2004. Carotid flow rates and flow division at the bifurcation in healthy volunteers. Physiol. Meas. 25 (3), 691–697. https://doi.org/10.1088/0967-3334/25/3/009.
- Mayfield Brain & Spine, 2022. Carotid Stenosis (Carotid Artery Disease). Https://Mayfieldclinic.Com/Pe-Carotidstenosis.Htm. https://mayfieldclinic.com/pe-carotidstenosis.htm.
- Mazzi, V., Gallo, D., Calò, K., Najafi, M., Khan, M.O., De Nisco, G., Steinman, D.A., Morbiducci, U., 2020. A Eulerian method to analyze wall shear stress fixed points and manifolds in cardiovascular flows. Biomech. Model. Mechanobiol. 19 (5), 1403–1423. https://doi.org/10.1007/s10237-019-01278-3.
- Moradicheghamahi, J., Jahangiri, M., Mousaviraad, M., Sadeghi, M.R., 2020. Computational studies of comparative and cumulative effects of turbulence, fluid–structure interactions, and uniform magnetic fields on pulsatile non-Newtonian flow in a patient-specific carotid artery. J. Braz. Soc. Mech. Sci. Eng. 42 (10), 1–22. https://doi.org/10.1007/s40430-020-02608-8.
- Morbiducci, U., Gallo, D., Massai, D., Ponzini, R., Deriu, M.A., Antiga, L., Redaelli, A., Montevecchi, F.M., 2011. On the importance of blood rheology for bulk flow in hemodynamic models of the carotid bifurcation. J. Biomech. 44 (13), 2427–2438. https://doi.org/10.1016/j.jbiomech.2011.06.028.
- Nagargoje, M., Gupta, R., 2020. Effect of sinus size and position on hemodynamics during pulsatile flow in a carotid artery bifurcation. Comput. Methods Prog. Biomed. 192, 105440 https://doi.org/10.1016/j.cmpb.2020.105440.
- Najjari, M.R., Plesniak, M.W., 2016. Evolution of vortical structures in a curved artery model with non-Newtonian blood-analog fluid under pulsatile inflow conditions. Exp. Fluids 57 (6), 1–16. https://doi.org/10.1007/s00348-016-2188-7.
- Nguyen, K.T., Clark, C.D., Chancellor, T.J., Papavassiliou, D., v., 2008. Carotid geometry effects on blood flow and on risk for vascular disease. J. Biomech. 41 (1), 11–19. https://doi.org/10.1016/j.jbiomech.2007.08.012.
- Park, J.H., Razuk, A., Saad, P.F., Telles, G.J.P., Karakhanian, W.K., Fioranelli, A., Rodrigues, A.C., Volpiani, G.G., Campos, P., Yamada, R.M., Castelli Jr., V., Caffaro, R.A., 2012. Carotid stenosis: what is the high-risk population? Clinics 67 (8), 865–870.
- Peiffer, V., Sherwin, S.J., Weinberg, P.D., 2013a. Does low and oscillatory wall shear stress correlate spatially with early atherosclerosis? A systematic review. Cardiovasc. Res. 99 (2), 242–250. https://doi.org/10.1093/cvr/cvt044.
- Peiffer, V., Sherwin, S.J., Weinberg, P.D., 2013b. Computation in the rabbit aorta of a new metric - the transverse wall shear stress - to quantify the multidirectional character of disturbed blood flow. J. Biomech. 46 (15), 2651–2658. https://doi.org/ 10.1016/j.jbiomech.2013.08.003.
- Perktold, K., Resch, M., Peter, R., 0., 1991. Three-dimensional numerical analysis of pulsatile flow and wall shear stress in the carotid artery bifurcation. J. Biomech. 24 (6), 409–420.
- Peterson, S.D., Plesniak, M.W., 2008. The influence of inlet velocity profile and secondary flow on pulsatile flow in a model artery with stenosis. J. Fluid Mech. 616, 263–301. https://doi.org/10.1017/S0022112008003625.
- Phan, T.G., Beare, R.J., Jolley, D., Das, G., Ren, M., Wong, K., Chong, W., Sinnott, M.D., Hilton, J.E., Srikanth, V., 2012. Carotid artery anatomy and geometry as risk factors for carotid atherosclerotic disease. Stroke 43 (6), 1596–1601. https://doi.org/ 10.1161/STROKEAHA.111.645499.
- Ravensbergen, J., Ravensbergen, J.W., Krijger, J.K.B., Hillen, B., Hoogstraten, H.W., 1998. Localizing role of hemodynamics in atherosclerosis in several human vertebrobasilar junction geometries. Arterioscler. Thromb. Vasc. Biol. 18 (5), 708–716. http://ahajournals.org.

- Rouleau, L., Farcas, M., Tardif, J.C., Mongrain, R., Leask, R.L., 2010. Endothelial cell morphologic response to asymmetric stenosis hemodynamics: effects of spatial wall shear stress gradients. J. Biomech. Eng. 132 (8) https://doi.org/10.1115/1.4001891, 081013.1-081013.10.
- Spanos, K., Petrocheilou, G., Karathanos, C., Labropoulos, N., Mikhailidis, D., Giannoukas, A., 2017. Carotid bifurcation geometry and atherosclerosis. Angiology 68 (9), 757–764. https://doi.org/10.1177/0003319716678741.
- Steinman, D.A., Robarts, J.P., Milner, J.S., Moore, J.A., Rutt, B.K., 1997. Hemodynamics of Human Carotid Artery Bifurcations: Computational Studies with Models Reconstructed from Magnetic Resonance Imaging of Normal Subjects.
- Stroud, J.S., Berger, S.A., Saloner, D., 2002. Numerical analysis of flow through a severely stenotic carotid artery bifurcation. J. Biomech. Eng. 124 (1), 9–20. https:// doi.org/10.1115/1.1427042.
- Tada, S., Tarbell, J.M., 2005. A computational study of flow in a compliant carotid bifurcation-stress phase angle correlation with shear stress. Ann. Biomed. Eng. 33 (9), 1202–1212. https://doi.org/10.1007/s10439-005-5630-1.

- Tada, S., Tarbell, J.M., 2005. A computational study of flow in a compliant carotid bifurcation - stress phase angle correlation with shear stress. Annals of biomedical engineering 33, 1202–1212.
- Thomas, J.B., Antiga, L., Che, S.L., Milner, J.S., Steinman, D.A.H., Spence, J.D., Rutt, B. K., Steinman, D.A., 2005. Variation in the carotid bifurcation geometry of young versus older adults: implications for geometric risk of atherosclerosis. Stroke 36 (11), 2450–2456. https://doi.org/10.1161/01.STR.0000185679.62634.0a.
- Wang, C., Baker, B.M., Chen, C.S., Schwartz, M.A., 2013. Endothelial cell sensing of flow direction. Arterioscler. Thromb. Vasc. Biol. 33 (9), 2130–2136.
- Zalud, N.C., Bulusu, K.V., Plesniak, M.W., 2022. Simulation of a Pro-Atherogenic High-Risk Carotid Artery Bifurcation Geometry. Bulletin of the American Physical Society. https://meetings.aps.org/Meeting/DFD22/Session/U05.3.
- Zhou, X., Yin, L., Xu, L., Liang, F., 2020. Non-periodicity of blood flow and its influence on wall shear stress in the carotid artery bifurcation: an in vivo measurement-based computational study. J. Biomech. 101, 109617 https://doi.org/10.1016/j. jbiomech.2020.109617.